Monthly Notices
of the
ROYAL ASTRONOMICAL SOCIETY

MNRAS **545,** 1–16 (2026) https://doi.org/10.1093/mnras/staf2222
Advance Access publication 2025 December 18

FRB 20240619D: a study of the hyperactivity, rotation measure evolution, and searches for a persistent radio source

Kavya Shaji [1,2,3]★ Jun Tian [4] Manisha Caleb [1,2] Kaustubh Rajwade [5] Ben Stappers [4] Inés Pastor-Marazuela [4,6] Tara Murphy [1,2] Ewan Barr [7] Ashna Gulati [1,2,3] Fabian Jankowski [8] Michael Kramer [7] Yu Wing Joshua Lee [1,2,3] and Pavan Uttarkar [9]

[1] *Sydney Institute for Astronomy, School of Physics, The University of Sydney, Sydney, NSW 2006, Australia*
[2] *ARC Centre of Excellence for Gravitational Wave Discovery (OzGrav), Hawthorn, VIC 3122, Australia*
[3] *Australia Telescope National Facility, CSIRO, Space & Astronomy, PO Box 76, Epping, NSW 1710, Australia*
[4] *Jodrell Bank Centre for Astrophysics, Department of Physics and Astronomy, The University of Manchester, Manchester M13 9PL, UK*
[5] *Astrophysics, The University of Oxford, Denys Wilkinson Building, Keble Road, Oxford OX1 3RH, UK*
[6] *ASTRON, the Netherlands Institute for Radio Astronomy, Oude Hoogeveensedijk 4, NL-7991 PD Dwingeloo, the Netherlands*
[7] *Max-Planck-Institut für Radioastronomie, Auf dem Hügel 69, D-53121 Bonn, Germany*
[8] *LPC2E, OSUC, Univ Orleans, CNRS, CNES, Observatoire de Paris, F-45071 Orleans, France*
[9] *Centre for Astrophysics and Supercomputing, Swinburne University of Technology, Hawthorn, VIC 3122, Australia*

Accepted 2025 December 12. Received 2025 December 9; in original form 2025 August 5

ABSTRACT

This paper presents a comprehensive wideband study of FRB 20240619D focusing on its hyperactivity, rotation measure evolution, and the search for an associated persistent radio source. Using data from the MeerKAT, Murriyang, and Lovell telescopes, we analysed the spectral, temporal, and polarimetric properties of 1539 bursts. Our observations reveal a remarkably high burst rate of 161 bursts per hour in early August above a fluence value of 1.6 Jy ms as well as significant secular variations in rotation measure and diverse polarization characteristics, including high linear polarization fractions and occasional circular polarization. The burst activity also showed frequency dependence with approximately 61 per cent of the total number of bursts detected between 1300 and 1800 MHz. The burst activity of FRB 20240619D ceased abruptly after a period of intense activity lasting approximately 80 d, suggesting an episodic behaviour. Follow-up observations with MeerKAT and Australia Telescope Compact Array did not reveal an associated compact persistent radio source. Altogether, our results highlight the importance of continued long-term monitoring and multiwavelength observations in understanding the emission mechanisms and diversity of progenitor populations of fast radio bursts.

Key words: methods: data analysis – methods: observational – techniques: interferometric – fast radio bursts.

1 INTRODUCTION

Fast radio bursts (FRBs) are coherent radio pulses lasting microseconds to milliseconds in duration and originating from extragalactic to cosmological distances (D. R. Lorimer et al. 2007; D. Thornton et al. 2013). These bursts experience a frequency-dependent time delay when they propagate through the ionized interstellar and intergalactic medium, which is quantified by the dispersion measure (DM). The DM represents the integrated electron column density along the line of sight, and all FRBs exhibit DMs significantly exceeding the Milky Way's contribution, indicating an extragalactic origin. Although most FRBs are observed as one-off events, ∼3 per cent of the population has been observed to repeat (CHIME/FRB Collaboration 2023). Currently, it is unclear whether repeating and non-repeating FRBs constitute distinct populations arising from different progenitors (M. Caleb et al. 2019; CHIME/FRB Collaboration 2023; F. Kirsten et al. 2024). However, morphological studies have shown that repeating FRBs exhibit statistically distinct burst characteristics compared to non-repeaters, such as broader pulse widths and narrower emission bandwidths (Z. Pleunis et al. 2021b).

Repeating FRBs are powerful tools for probing their emission mechanisms, as repeat bursts allow precise localization and detailed studies of their host environments. However, a unified study is currently challenging due to significant differences in their activity levels, spectro-temporal properties, and host environments. Some sources, known as hyperactive repeaters, such as FRB 20121102A (D. Li et al. 2021; D. M. Hewitt et al. 2022; J. N. Jahns et al. 2023), FRB 20201124A (A. E. Lanman et al. 2022), and FRB 20240114A (A. Kumar, Y. Maan & Y. Bhusare 2024b; U. Panda et al. 2024; J. Tian et al. 2024a; K. Shin et al. 2025), exhibit exceptionally high burst rates, emitting tens to hundreds of bursts per hour, far exceeding typical repeater activity. These bursts often cluster in time. For example, FRB 20180916B and FRB 20121102A exhibit periodic activity, with bursts confined to specific windows in each cycle (CHIME/FRB Collaboration 2020; K. M. Rajwade et al. 2020;

★ E-mail: ksha0606@uni.sydney.edu.au

M. Cruces et al. 2021; C. A. Braga et al. 2025), possibly linked to orbital (K. Ioka & B. Zhang 2020), rotational (P. Beniamini, Z. Wadiasingh & B. D. Metzger 2020), or precessional (Y. Levin, A. M. Beloborodov & A. Bransgrove 2020) periods. It is also noteworthy that the observing window of FRB 20180916B shifts as a function of frequency (Z. Pleunis et al. 2021a; S. Bethapudi et al. 2023). In contrast, hyperactive repeaters like FRB 20220921A show no evidence of periodicity (D. M. Hewitt et al. 2023; Y.-K. Zhang et al. 2023; Y. Feng et al. 2024), which underscores the diversity in repeating behaviours. Follow-up observations of these hyperactive repeaters have yielded large samples of burst detections revealing important features such as the evolution of burst activity with time (e.g. I. Pastor-Marazuela et al. 2021; A. E. Lanman et al. 2022), the evolution of linear polarization position angle (PPA) with time (R. Luo et al. 2020), and depolarization towards lower frequencies (Y. Feng et al. 2022). Some repeating FRBs are also known to show a spectral variation in their emission activity, with their preferred emission frequency shifting over hours to days (P. Kumar et al. 2022; A. V. Bilous et al. 2025). The different activity characteristics of repeating FRBs offer important clues about the diversity of their central engines and local environments, suggesting that multiple physical mechanisms or evolutionary stages may be at play, making them essential to study to uncover the full landscape of FRB progenitors.

Repeating FRBs also exhibit a variety of polarization properties, including high linear polarization fractions near 100 per cent (V. Gajjar et al. 2018; J. M. Cordes & S. Chatterjee 2019; E. Fonseca et al. 2020), occasional circular polarization (J.-C. Jiang et al. 2022; P. Kumar et al. 2022), and diverse PPA variabilities such as S-shaped swings (X. Liu et al. 2025), orthogonal jumps (J. R. Niu et al. 2024), and flat PPAs (D. Michilli et al. 2018; P. Kumar et al. 2021a). Rotation measure (RM), which quantifies the Faraday rotation of polarized light through magnetized plasma, provides clues into the magnetic fields and electron densities around FRBs. Recent studies (R. Mckinven et al. 2023b; C. Ng et al. 2025) have highlighted the variation in RM as an intriguing feature of repeating FRBs. Some repeaters exhibit secular RM variation, while others display more complex behaviour, including stochastic RM variations followed by secular increases or intervals of secular RM evolution (D. Michilli et al. 2018; G. H. Hilmarsson et al. 2021; R. Anna-Thomas et al. 2023; R. Mckinven et al. 2023b; A. Kumar et al. 2024b; C. Ng et al. 2025). These diverse polarization and RM behaviours again point to significant differences in the local magneto-ionic environments and magnetic field structures, reflecting the complexity and possible diversity of progenitor systems of repeating FRBs.

In addition to burst properties and polarization behaviour, the multiwavelength counterparts of repeating FRBs offer additional insights into their origins and local environments. Some repeating FRBs are associated with persistent radio sources (PRSs), long-lived radio continuum sources with luminosities exceeding those expected from star formation in their host galaxies. To date, five FRBs have been linked to PRSs: FRB 20121102A , FRB 20190520B, FRB 20201124A, FRB 20240114A, and FRB 20190417A (S. Chatterjee et al. 2017; C. H. Niu et al. 2022; G. Bruni et al. 2024, 2025; Y. Bhusare, Y. Maan & A. Kumar 2025; A. M. Moroianu et al. 2025; X. Zhang et al. 2025). Theoretical models suggest a relation between PRS luminosity and the RM of associated FRBs (Y.-P. Yang, Q.-C. Li & B. Zhang 2020). Observations of FRBs 20121102A and 20190520B, both associated with bright PRSs, confirm this connection through their high RM (D. Michilli et al. 2018; C. H. Niu et al. 2022). The most promising explanation for the association between FRBs and PRSs is the magnetar-powered synchrotron maser shock model. In this model, FRBs are produced by synchrotron maser emission from decelerating relativistic magnetized shocks, while the PRS arises from synchrotron radiation emitted by the magnetar's surrounding wind nebula (B. Margalit & B. D. Metzger 2018; B. D. Metzger, B. Margalit & L. Sironi 2019). Magnetars can account for many FRB properties, including energetics and polarization (B. D. Metzger et al. 2019; R. Luo et al. 2020), but they do not fully explain the diversity of repetition rates, burst morphologies, polarization behaviour, or periodic activity. Thus, discovering and monitoring more repeating FRBs over long timescales and across wide frequency bands is essential for revealing their diversity. These efforts will help in clarifying how they relate to the broader FRB population, including non-repeaters, and constraining progenitor models and the physical processes driving the bursts. This paper presents wideband monitoring of the hyperactive repeater FRB 20240619D, providing a high-cadence data set that reveals key insights into the temporal and spectral evolution of its bursts, along with a search for a PRS, advancing our understanding of repeating FRBs.

FRB 20240619D was first discovered by the MeerTRAP (More TRansients And Pulsars) project (K. M. Rajwade et al. 2022; F. Jankowski et al. 2023) on 2024 June 19 (J. Tian et al. 2025). The initial discovery included three bursts observed within 2 min at L band (856–1712 MHz) with a structure maximizing DM of 464.85 ± 0.01 pc cm^{-3} (J. Tian et al. 2025). Subsequent detections from MeerKAT, the Westerbork RT-1 25-m telescope (O. S. Ould-Boukattine et al. 2025a), and the upgraded Giant Metrewave Radio Telescope (A. Kumar et al. 2024c) confirmed the source's hyperactivity. In this paper, we report the follow-up analysis of spectro-temporal properties, polarization properties, burst activity, and a PRS search for FRB 20240619D using data from MeerKAT, Murriyang, Lovell, and Australia Telescope Compact Array (ATCA). In Section 2, we describe observations and data reduction results of our follow-up. We discuss our findings and implications in Section 3. Finally, we conclude our analyses in Section 4.

2 OBSERVATIONS, DATA PROCESSING, AND RESULTS

2.1 Searches for a persistent radio source with MeerKAT

FRB 20240619D was localized by J. Tian et al. (2025) using MeerKAT to a position of RA = 19:49:29.2±0.9 arcsec and Dec. = −25:12:49.6±0.9 arcsec, which was subsequently adopted as the reference position for our follow-up observations with MeerKAT, Murriyang, Lovell, and ATCA. Observations with MeerKAT consist of both interferometric and beamformed modes, which include 1 h at L band (856–1712 MHz) and 1 h at S band (1968–2843 MHz) on 2024 June 26 as part of a Director's Discretionary Time proposal (proposal ID: DDT-20240625-JT-01). Further follow-up was performed using the MeerKAT in the simultaneous dual-frequency subarray mode in ultra-high frequency (UHF; 544–1088 MHz) and L band on 2024 June 28. An additional follow-up was conducted on 2024 September 20, at L band using the entire array. In all instances, the correlator data were recorded with an integration time of 2 s. J1939−6342 and J1924−2914 were used as the primary and secondary calibrators for all the observations. Along with the imaging data, the simultaneously recorded beamforming data for the first four MeerKAT observations in June were searched for bursts (J. Tian et al. 2025). The details of the observation and the number of bursts detected in the corresponding observations are listed in Table 1.

Table 1. Summary of MeerKAT observations of FRB 20240619D. This table provides details, including the UTC date, observation time, frequency band, array configuration, number of antennas, maximum baseline length, angular resolution, and the number of bursts detected. The observations were conducted in 2024 June and September, using both full array and subarray modes across different frequency bands.

Date	Time (h)	Frequency band (MHz)	Array	Number of antennas	Max baseline (km)	Angular resolution (arcsec)	Bursts detected
2024 June 26	1.29	L (856–1712)	Full array	44	1.24	38.9	69
2024 June 26	1.30	S (1968–2843)	Full array	43	1.13	22.9	26
2024 June 28	2.30	UHF (544–1088)	Subarray	30	7.6	10.0	44
2024 June 28	2.30	L (856–1712)	Subarray	32	7.7	6.3	144
2024 Sept 20	1.30	L (856–1712)	Full array	61	7.8	6.2	0

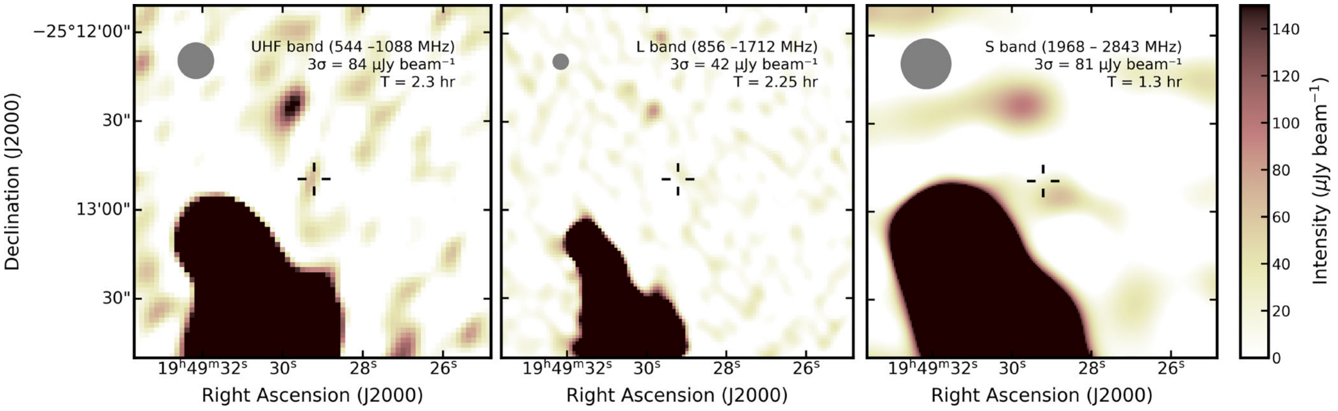

Figure 1. MeerKAT continuum images of the field around FRB, at different observing epochs and frequencies (Table 1). The three panels represent images from L band (2024 June 28), UHF band (2024 June 28), and S band (2024 June 26), respectively. The black cross-hair marks the FRB position with a 3σ positional uncertainty ($1\sigma = 0.9$ arcsec in RA and Dec.; J. Tian et al. 2024b). The grey ellipse in the top-left corner represents the synthesized beam. The colour scale shows the intensity in μJy beam^{-1}. The images have been cropped to a common 60×60 pixels region centred on the FRB position RA: 19:49:29.21, Dec.: −25:12:49.64. The colour scale for the intensity is normalized to a maximum value of 150 μJy beam^{-1} for comparison across the panels. An extended radio source, AGN J194930.09−251338.6, identified from the Million Quasars Catalog (E. W. Flesch 2015), is located approximately 50 arcsec away from the FRB location and appears as the bright source to the bottom-left of the FRB position. The S-band observation included only antennas from the central core of the array, resulting in poor resolution as seen in the last panel (see Table 1 for details on the observing details with MeerKAT).

To identify the presence of a compact PRS potentially associated with FRB 20240619D, we performed imaging on all observations across the L, S, and UHF bands. Calibration and imaging were performed using the OXKAT[1] pipeline (I. Heywood 2020). We used the default `1GC`, `FLAG`, `2GC`, and `3GC` settings for imaging, which automatically produced high-quality full-band continuum images. Flux density measurements were performed on these full-band continuum images using PYBDSF[2] (N. Mohan & D. Rafferty 2015). We performed imaging on the L-band observation from 2024 June 28, after removing the 144 bursts detected during the observation (Table 1). These bursts were removed using the `flagdata` task in CASA (Common Astronomy Software Applications; J. P. McMullin et al. 2007), after accounting for their dispersive delay of 1.9 s at L band for a DM of 464.85 pc cm^{-3}. The flagging of the bursts resulted in the removal of 3.3 per cent of the total data from the full 2.3-h observation. Without removing these 144 bursts, the integrated flux density at the source position was measured to be 90 μJy beam^{-1}. No compact radio continuum source was detected above a threshold of 3σ [where σ denotes the image root mean square (rms) noise] at the position of the FRB in the L, S, and UHF bands. This non-detection applies within the $15\sigma_{\rm pos}$ confidence region of the FRB location, where $\sigma_{\rm pos}$ refers to the uncertainty in the FRB localization. See Fig. 1 and Tables 1 and 2 for observation details and imaging results.

2.2 Searches for a persistent radio source with ATCA

If synchrotron emission from an ion–electron medium produces the PRS associated with existing FRBs, models (B. Margalit & B. D. Metzger 2018) predict that such emission peaks at radio frequencies above ∼1 GHz, with a self-absorption turnover occurring in the ∼1.6–6 GHz range depending on the specific model parameters. Hence, we searched for a PRS coincident with the localized position of FRB 20240619D using the ATCA at frequencies centred at 5500 and 7500 MHz (*C* and *X* band), with a bandwidth of 2048 MHz for each intermediate centre frequency. The observations, conducted on 2024 December 16, used a spectral resolution of 1 MHz and a total integration time of 3 h in the 5A configuration. The Compact Array Broadband Backend (CABB; W. E. Wilson et al. 2011) was used for the observations, with sources PKS B1934−638 and PKS B1921−293 used as the flux and phase calibrators, respectively.

The correlated data from CABB were processed using MIRIAD (R. J. Sault, P. J. Teuben & M. C. H. Wright 1995). Radio frequency interference (RFI) flagging was performed using the MIRIAD utilities BLFLAG and PGFLAG. Deconvolution was performed on individual intermediate frequencies of 5.5 and 7.5 GHz. No compact continuum emission was detected at the FRB 20240619D's localization in either the C or X bands. For the ATCA images, we used the `imfit` task

---

[1] https://github.com/IanHeywood/oxkat/blob/92172ade956dd6abcf0f6dc0bc9ff3fd5c4eab12/README.md
[2] https://pybdsf.readthedocs.io/

Table 2. rms noise and 3σ upper limits on the flux density of the potential PRS from MeerKAT and ATCA observations. Of the three MeerKAT L-band observations conducted on 26 June, 28 June, and 20 September (see Table 1), only the 28 June observation, which had the lowest rms noise, was used to calculate the flux density upper limit at L band shown in this table.

Telescope	Date	Frequency band	Integration time (h)	rms (µJy beam^{-1})	3σ upper limit (µJy beam^{-1})
MeerKAT	2024 June 26	S (1968–2843 MHz)	1.30	27	81
MeerKAT	2024 June 28	L (856–1712 MHz)	2.25	14	42
MeerKAT	2024 June 28	UHF (544–1088 MHz)	2.30	28	84
ATCA	2024 Dec 16	C (4.4–6.7 GHz)	3.00	400.8	1202.4
ATCA	2024 Dec 16	X (7.5–10.5 GHz)	3.00	300.6	901.8

Table 3. Summary of Murriyang observations of FRB 20240619D. This table lists the UTC dates, observation times, and the total number of bursts detected across the 704–4032 MHz frequency range during the monitoring period from 2024 August to 2024 December. We summarize the number of bursts used for DM and RM estimation in the fourth and fifth columns. The last two columns list the median RM and DM values for each day, weighted by the measurement errors, along with the corresponding 1σ uncertainty, where available. We estimated the uncertainties in median DM and median RM using a parametric bootstrap method applied to the bursts selected for RM and DM determination. Only bursts with an S/N greater than 20 were used for DM and RM estimation, and only bursts with significant linear polarization were used for RM determination.

Date	Time (h)	Total number of bursts	Number of bursts used for RM	Number of bursts used for DM	Weighted median RM (rad m^{-2})	Weighted median DM (pc cm^{-3})
2024 Aug 03	2.43	219	13	9	−253.7 ± 1.0	463.2 ± 0.4
2024 Aug 05	2.42	389	29	9	−264.2 ± 5.5	466.8 ± 0.3
2024 Aug 08	1.95	265	6	3	−245.2 ± 1.9	463.2 ± 0.6
2024 Aug 10	1.86	218	22	5	−290.4 ± 2.5	466.0 ± 0.4
2024 Aug 20	1.00	10	1	1	−272.5 ± 18.2	467.9 ± 1.2
2024 Aug 31	1.05	6	–	2	–	464.9 ± 1.0
2024 Sept 01	0.94	3	1	1	−300.9 ± 0.6	465.9 ± 0.8
2024 Sept 02	0.87	6	1	1	−301.8 ± 3.0	465.9 ± 1.1
2024 Sept 03	0.92	18	2	5	−297.7 ± 0.7	467.3 ± 0.7
2024 Sept 04	0.93	5	1	1	−291.5 ± 3.9	464.3 ± 1.0
2024 Sept 16	1.00	0	–	–	–	–
2024 Sept 20	1.00	0	–	–	–	–
2024 Sept 27	1.00	0	–	–	–	–
2024 Sept 30	1.00	0	–	–	–	–
2024 Nov 12	0.82	0	–	–	–	–
2024 Nov 24	1.00	0	–	–	–	–
2024 Nov 29	0.43	0	–	–	–	–
2024 Dec 04	1.00	0	–	–	–	–
2024 Dec 10	0.30	0	–	–	–	–

within the MIRIAD software package to measure the rms noise and computed the 3σ upper limits on the flux density of the PRS (Table 2). The rms noise level was found to be 400.8 µJy beam^{-1} in the *C* band (4.8–9.6 GHz), corresponding to a 3σ upper limit on the PRS flux density of 1202.4 µJy beam^{-1}. In the *X* band (8.0–12.0 GHz), the rms noise level was 300.6 µJy beam^{-1}, yielding a 3σ upper limit of 901.8 µJy beam^{-1}. Due to the use of only five antennas and a limited 3-h integration, the resulting elongated beam and sparse ultraviolet coverage led to poor image quality, so the images from ATCA are not shown in this paper.

2.3 Murriyang and Lovell observations

2.3.1 Murriyang observations

FRB 20240619D was observed for repeat bursts using the ultrawide bandwidth low-frequency (UWL) receiver on the 64-m Murriyang radio telescope covering a continuous frequency range from 704 to 4032 MHz (G. Hobbs et al. 2019). The source was monitored for a total of 18 h between 2024 August and 2024 December. The data were recorded in the pulsar search mode with a spectral resolution of 1 MHz (3328 channels across the whole band) and a sampling time of 256 µs. Data were stored in an 8-bit sampled PSRFITS search mode file (A. W. Hotan, W. van Straten & R. N. Manchester 2004) with full Stokes data. We performed a comprehensive search of these wideband data using a subband search pipeline, using HEIMDALL (B. R. Barsdell 2012) and FETCH (D. Agarwal et al. 2020). See P. Kumar et al. (2021b) for a detailed description of the search pipeline. Data were searched in a DM range of $400 \le \mathrm{DM} \le 500$ pc cm^{-3} with a step size of 0.1 pc cm^{-3} and a maximum boxcar width of 100 ms. The frequency range of 704–4032 MHz was divided into multiple subbands with bandwidths of 64, 128, 256, 512, 832, 1664, and 3328 MHz for single-pulse searches, including overlapping subbands to avoid missing pulses at the band edges. We visually inspected each of the FETCH classified candidates. Our search resulted in 1138 promising candidates above a signal-to-noise ratio (S/N) of 7, as detailed in Table 3, with the last detection on 2024 September 4. Follow-up observations conducted with Murriyang from 2024 September 16 to 2024 mid-December yielded no further burst detections.

Fig. 2 displays a subset of the 1138 bursts detected with Murriyang, exhibiting a variety of temporal, spectral, and polarimetric properties. Bursts M51, M246, and M1090 exhibit narrow pulse widths with high linear polarization fractions and minimal circular polarization.

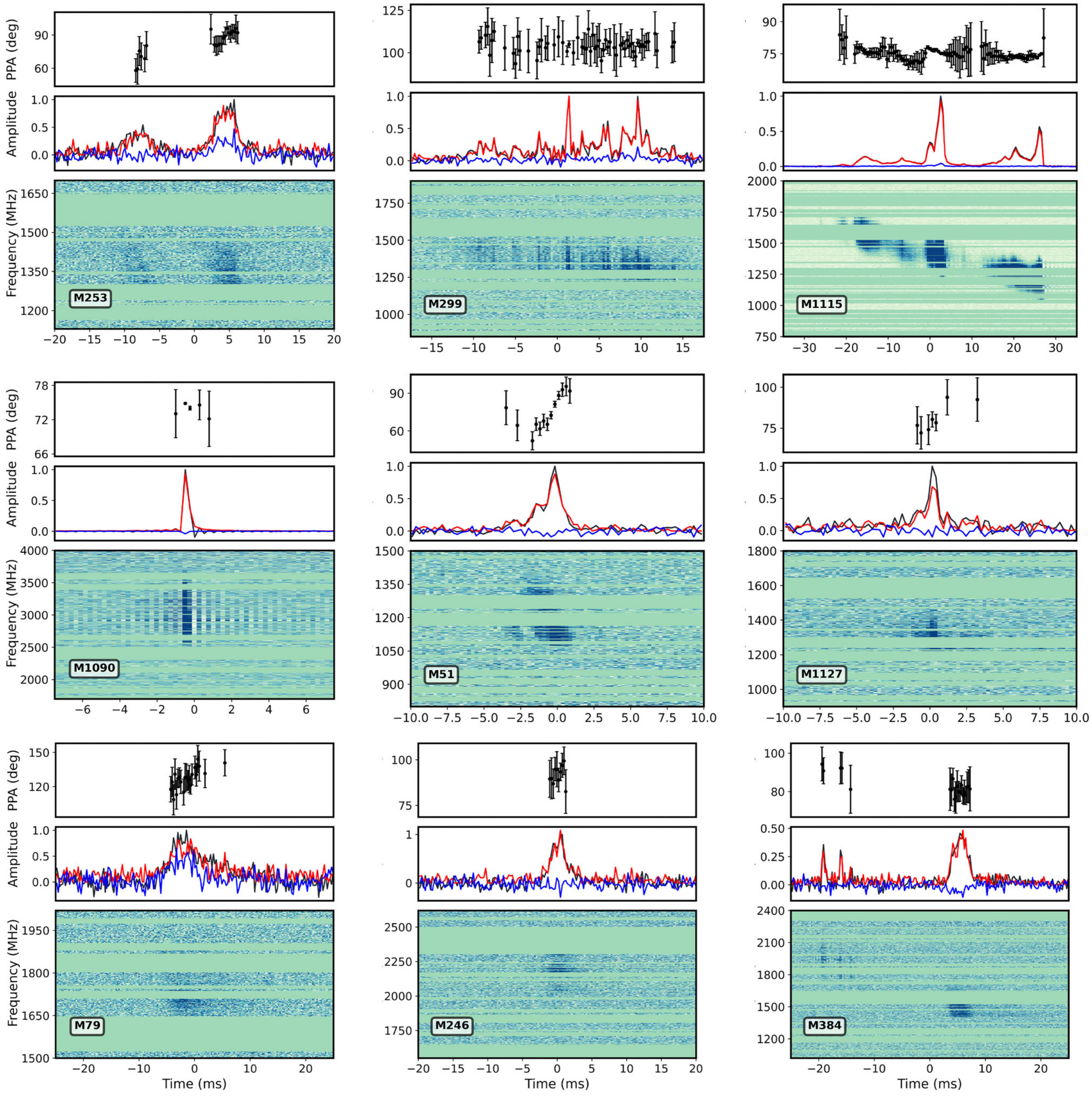

Figure 2. PPA, pulse profile, and dynamic spectra of nine individual bursts from FRB 20240619D observed with Murriyang. The top panel displays the PPA of the linear polarization as a function of time, and the middle panel shows the Stokes parameters: total intensity (I, black), linear polarization fraction (L/I, red), and circular polarization fraction (V/I, blue), normalized to the peak intensity. The bottom panel presents the dynamic spectrum, and horizontal lines with uniform colouring indicate channels flagged due to RFI. The filterbank data are dedispersed to 464.85 pc cm^{-3}, which is the structure-maximizing DM reported in J. Tian et al. (2025). This value was used because no measurable DM evolution was observed (see Section 2.3.4).

Notably, burst M1090 is exceptionally narrow, being only one time bin wide ($\leq$256 μs). It is also very bright, causing the ripples in Fig. 2, which are artefacts due to saturation and a non-linear response in the digitizer. M253, M299, M384, and M1115 exhibit multiple and complex subbursts, with a subset of them also displaying downward drifting frequency structures. The bursts in this figure highlight the diversity in morphology, polarization fractions, spectral occupancy, and PPA behaviour across the sample of Murriyang bursts.

2.3.2 *Lovell observations*

We followed up FRB 20240619D with the Lovell telescope from MJD 60493 to 60585. The observations were processed through the ROACH backend, which used a polyphase filterbank to channelize the data recorded between 1396 and 1732 MHz into 21 × 16 MHz subbands. Then each subband was further channelized into 32 × 0.5 MHz channels with a sampling time of 256 μs using DSPSR. We

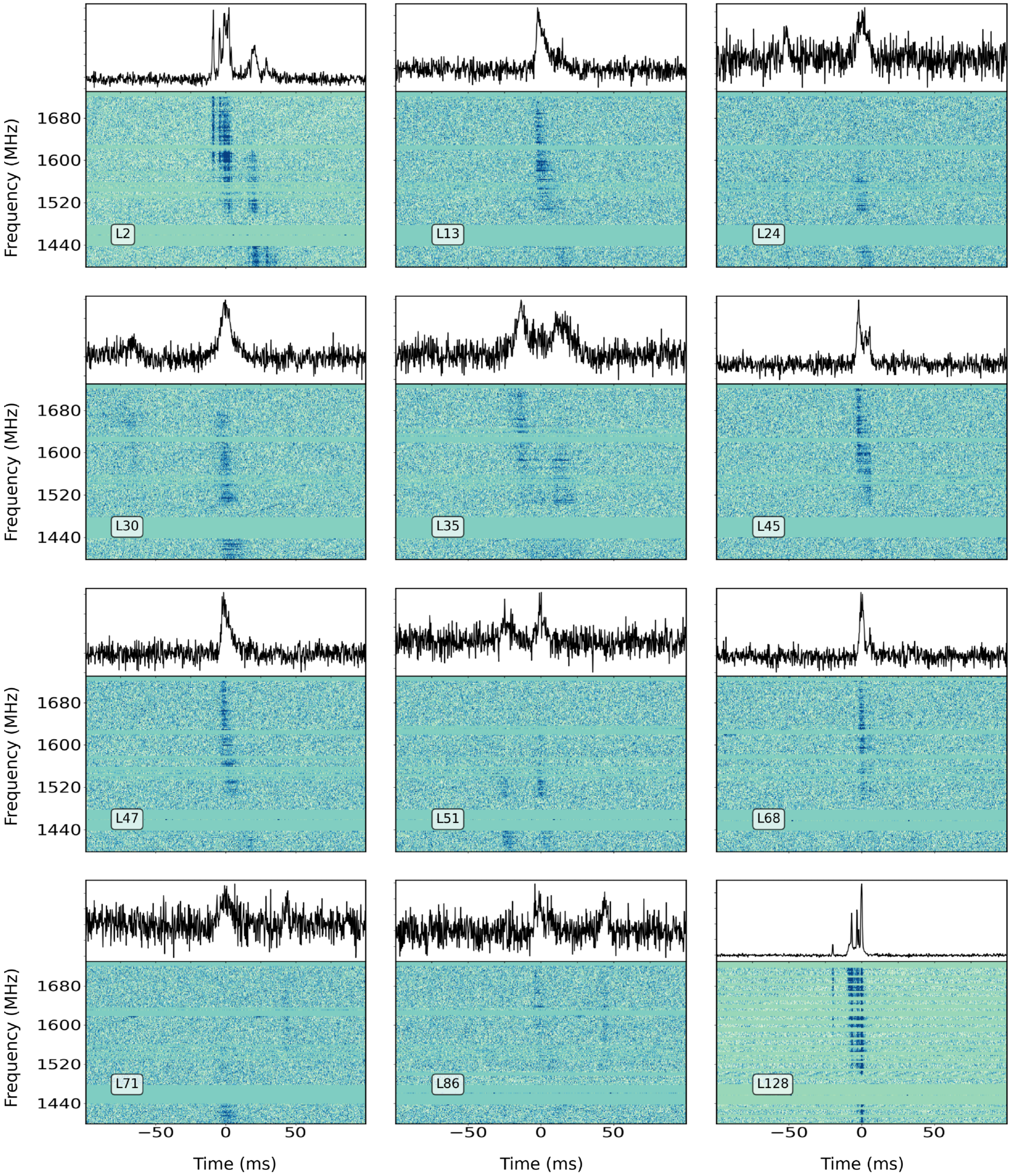

Figure 3. A selection of bursts detected from FRB 20240619D using the Lovell telescope. This sample includes bright bursts or those with multiple subcomponents and/or complex time–frequency structures. Each panel illustrates the dynamic spectrum of bursts (Table 4) plotted from filterbank data dedispersed to 464.85 pc cm^{-3}. The top subpanel displays the frequency-averaged pulse profile in arbitrary units.

Table 4. Summary of Lovell observations of FRB 20240619D bursts. This table lists the UTC dates, observation durations, and the total number of bursts detected across the frequency range (704–4032 MHz) of UWL during the monitoring period from 2024 August to 2024 December. The final two columns list the number of bursts used and the median DM for each observation day, weighted by the individual burst uncertainties. The 1σ uncertainties on the median were estimated using a parametric bootstrap method. Note that only bursts with $S/N > 20$ are used for DM estimation.

Date	Time (h)	Total number of bursts	Number of bursts used for DM	Weighted median DM (pc cm^{-3})
2024 July 02	1	6	2	465.2 ± 1.4
2024 July 26	1	48	15	464.9 ± 0.5
2024 July 29	1	25	9	463.5 ± 0.6
2024 July 30	1	34	13	463.7 ± 0.5
2024 Aug 02	1.5	4	1	466.8 ± 1.5
2024 Aug 03	0.5	7	3	469.2 ± 1.1
2024 Aug 06	1	10	4	463.2 ± 1.0
2024 Aug 11	1	17	4	465.5 ± 0.9
2024 Aug 14	1	1	1	463.2 ± 1.3
2024 Aug 23	1	0	–	–
2024 Sept 06	1	0	–	–
2024 Oct 02	1	0	–	–

searched these observations for single pulses using TRANSIENTX[3] (Y. Men & E. Barr 2024). We chose a DM search range between 400 and 500 pc cm^{-3} with a step size of 0.1 pc cm^{-3} and a maximum boxcar width of 100 ms. Single-pulse events detected with an S/N above 7 were manually inspected for real signals. This resulted in the detection of 152 bursts, a subset of which is shown in Fig 3. The details of the Lovell observations are given in Table 4.

2.3.3 *Burst activity and burst properties*

As depicted in Fig. 4, approximately 73 per cent of all Murriyang-detected bursts were detected in early August, during which the burst rate reached a peak of around 161 bursts per hour. Approximately 61 per cent of the total number of bursts detected with Murriyang, Lovell, and MeerKAT fall between 1.3 and 1.8 GHz. For Murriyang alone, which provides a larger bandwidth, we find that about 58 per cent of the 1138 detected bursts fall between 1.3 and 1.8 GHz (Fig. 5). This suggests that the emission exhibits frequency dependence.

We compared the temporal widths and spectral bandwidths of bursts detected by the three telescopes: Murriyang, Lovell, and MeerKAT. The top panel of Fig. 6 illustrates the distribution of burst temporal widths. For Murriyang, we include only the 145 bursts with reliable measurements, excluding those affected by RFI. All three telescopes exhibit a comparable range of widths. Specifically, we found a median width of 4 ms ($\sigma = 11$ ms, where σ denotes the one standard deviation) for Murriyang, while both Lovell and MeerKAT displayed a median of 8 ms (with $\sigma = 10$ ms and $\sigma = 9$ ms, respectively).

The bottom panel of Fig. 6 shows the distribution of the spectral extents. Murriyang detected the widest range of spectral extents, with a median bandwidth of 109.2 MHz and a standard deviation of 159.3 MHz. Nearly 50 per cent of the bursts detected with Murriyang have bandwidths narrower than 100 MHz, indicating a preference for narrow-band emission that is detectable only because of the wide instantaneous coverage of the UWL receiver. In contrast, the Lovell telescope detected bursts with a median bandwidth of 99.8 MHz ($\sigma = 68.4$ MHz). This distribution is constrained by the receiver's instrumental bandwidth, which spans 1396–1732 MHz. Finally, we found that bursts detected with MeerKAT exhibit the largest spectral extents, with a median bandwidth of 251.8 MHz ($\sigma = 110.5$ MHz).

2.3.4 *Structure-maximizing DM estimation*

We used `DM_phase` (A. Seymour, D. Michilli & Z. Pleunis 2019) to measure the structure-maximizing DM of bursts from FRB 20240619D detected by Murriyang and Lovell. This algorithm determines DM by maximizing pulse phase coherence across frequency channels using a Fourier-based metric, enabling precise DM measurements for bursts with complex temporal structures. Approximately 3 per cent of Murriyang bursts and 34 per cent of Lovell bursts with $S/N > 20$ were used for DM measurements. Some of these bursts exhibited complex temporal structures, including multiple subcomponents and non-Gaussian profiles. We list the number of bursts chosen for DM determination in Table 3 for Murriyang and Table 4 for Lovell. The median DM values for each observation, weighted by their measurement uncertainties, are also summarized in these tables. We observed no significant DM evolution between 2024 June 26 and 2024 September 4, with the measurements remaining consistent with the 2024 June MeerKAT value of 464.85 ± 0.01 pc cm^{-3} (J. Tian et al. 2025). O. S. Ould-Boukattine et al. (2025a) reported an increase in DM of 0.41 ± 0.02 pc cm^{-3} over a 2-month period, from 2024 mid-July to mid-September, based on observations conducted with the Westerbork telescope of FRB 20240619D. Our measurements are not sensitive to such small DM variations due to the larger uncertainties associated with our DM measurements.

To evaluate this further, we combined the Murriyang (Table 3) and Lovell (Table 4) median DM measurements (weighted by the number of bursts per epoch) and fitted a simple linear model. From the profile-likelihood analysis, we obtained a best-fitting slope of $|\mathrm{dDM}/\mathrm{d}t| = 0.018 \pm 0.016$ pc cm^{-3} d^{-1}, consistent with no statistically significant evolution of DM given the scatter in our measurements. Using a frequentist 3σ criterion ($\Delta\chi^2 = 9$), we derive an upper limit of $|\mathrm{dDM}/\mathrm{d}t| < 0.38$ pc cm^{-3} d^{-1}. Here, χ^2 is the weighted sum of squared residuals between the measured DM values and the model, $\Delta\chi^2$ is the difference between χ^2 at a given slope and the minimum χ^2, and σ refers to the standard deviation of the slope estimate.

---

[3] https://github.com/ypmen/TransientX

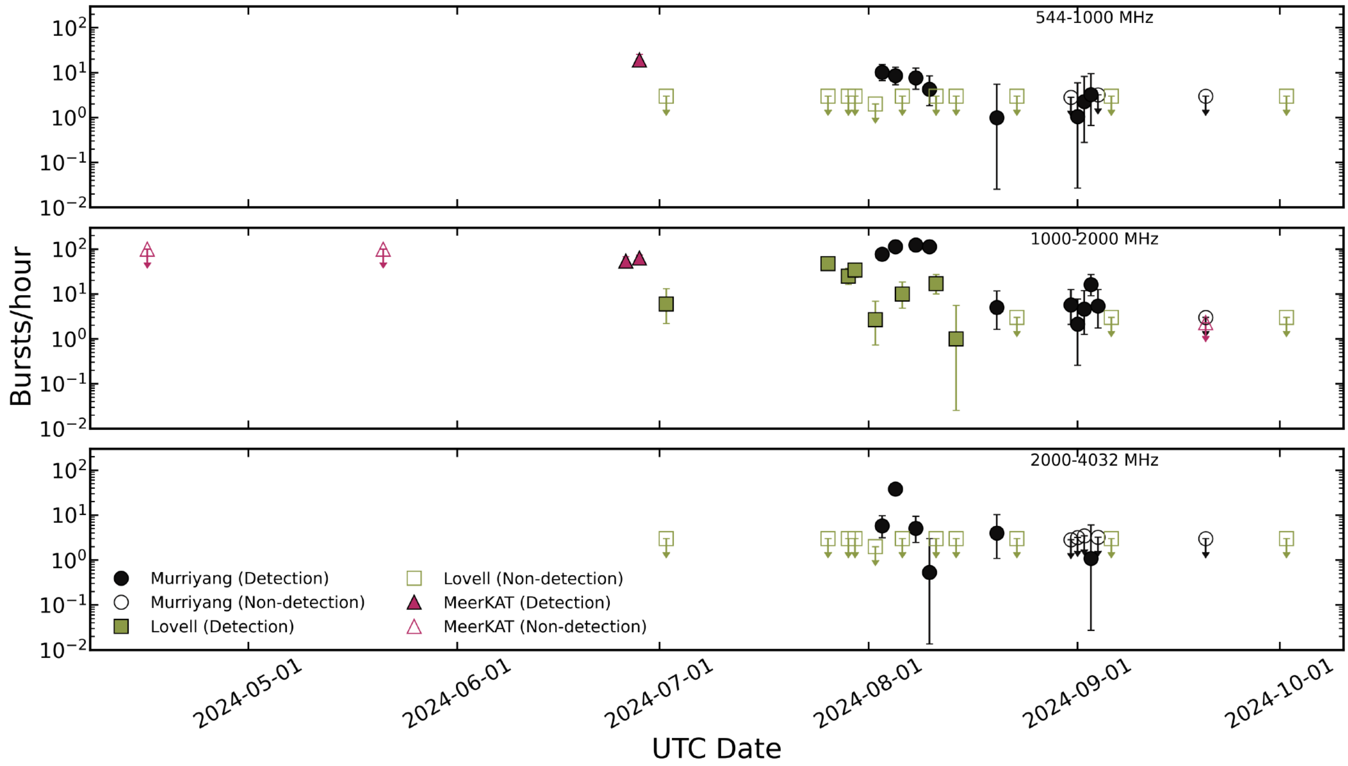

Figure 4. Temporal variation of the burst rate of FRB 20240619D as a function of UTC date across three distinct frequency bands: 544–1000 MHz, 1000–2000 MHz, and 2000–4032 MHz. These frequency divisions are chosen to avoid double-counting bursts that are simultaneously detected in overlapping frequency ranges across different telescopes. Observations were conducted with the Murriyang (circles), Lovell (squares), and MeerKAT (triangles) telescopes. Only bursts with fluence above 1.6 Jy ms are included in this plot. Filled markers denote detections with 95 per cent Poisson confidence intervals. Open markers with downward arrows indicate 95 per cent confidence upper limits for non-detections. Burst rates, expressed in bursts per hour, are derived from the total observation time and the number of bursts detected in each frequency band. See Tables 1, 3, and 4 for a summary of observation durations and burst counts.

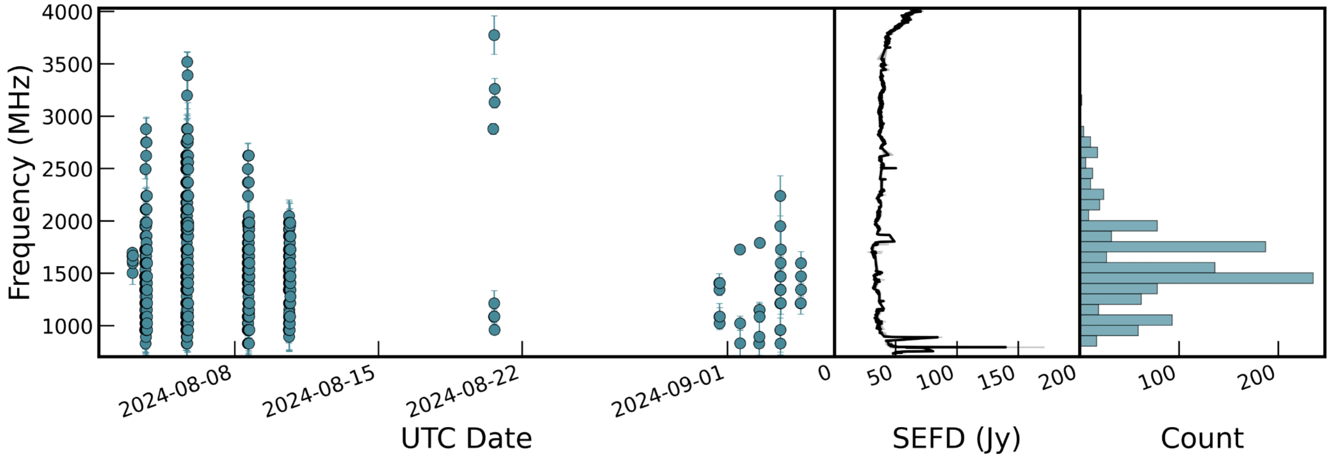

Figure 5. Burst frequency distribution of FRB 20240619D from Murriyang observations. Left panel: Burst frequency (in MHz) is plotted against the UTC date as observed with the Murriyang telescope. Error bars indicate the spectral extent, which is calculated by fitting a Gaussian function to the on-pulse spectrum. The spectral extent is defined as the width at 10 per cent of the maximum amplitude. Centre panel: The median system equivalent flux density (SEFD) in Jy is plotted across the frequency range 704–4032 MHz. We obtained the SEFD from Murriyang flux-calibration files downloaded from the Parkes Clock and CAL Files archive. For each frequency channel, we computed the median SEFD from calibration measurements taken on 2024 August 4, August 16, and September 3. We selected these dates as these were the nearest available calibration measurements during FRB 20240619D's active period, when bursts were detected above Murriyang's sensitivity threshold. The shaded region represents the interquartile range, indicating the variability in SEFD across observations. Right panel: A histogram of burst frequencies within the UWL band (704–4032 MHz) is shown, binned at 100 MHz intervals. The histogram represents the number distribution of bursts across the observed frequency range.

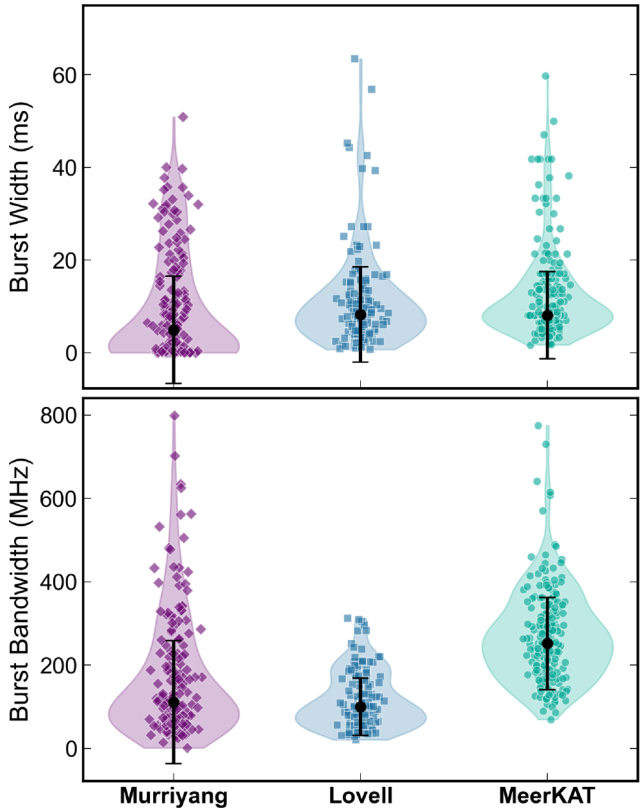

Figure 6. The distributions of burst temporal widths (top panel) and spectral extents (bottom panel) as violin plots for the Murriyang (diamonds), Lovell (squares), and MeerKAT (circles) telescopes. The shaded regions represent the kernel density estimation of the distributions, while scattered points show individual bursts. The points with vertical error bars represent the median ± one standard deviation.

2.3.5 Polarimetry and RM evolution

We created a full Stokes parameter PSRFITS format archive for the repeat bursts by extracting the UWL data using DSPSR (W. Straten & M. Bailes 2011). RFI excision was performed using the standard PAZI tool in PSRCHIVE (A. W. Hotan et al. 2004; W. Straten & M. Bailes 2011). The archives were then calibrated to measure the flux density and polarimetric properties following the procedures described in S. Dai et al. (2019) and M. E. Lower et al. (2020). Both flux and polarization calibration were performed using PSRCHIVE (A. W. Hotan et al. 2004; W. Straten & M. Bailes 2011). The flux calibration was done using the flux calibrator 1948–068 and polarization calibration was performed using a 2-min observation of a linearly polarized noise diode at the start of every observation.

We used the RMSYNTH tool from the PSRSALSA[4] software suite to search for the Faraday rotation in the Stokes data. We conducted a broad RM search within ±10 000 $\mathrm{rad\,m^{-2}}$, using a step size of 0.1 $\mathrm{rad\,m^{-2}}$. Out of the 1138 bursts detected by Murriyang, only 80 bright bursts ($\mathrm{S/N} > 20$) resulted in RM measurements. The median RMs for each epoch are listed in Table 3.

For all bursts that resulted in an RM measurement, we derotated for the Faraday rotation using the corresponding RM. After derotation, we used PSRSALSA to measure their polarization fraction and PPA over time. Specifically, we used PMOD to remove the baseline of the Stokes parameters and PPOL to calculate the linear polarization intensity $L = \sqrt{Q^2 + U^2}$ and PPA. Bias in L was removed for each sample using the method from J. F. C. Wardle & P. P. Kronberg (1974). A 3σ threshold on the debiased L was used to determine significant PPA measurements. A subset of polarimetric pulse profiles and significant PPA measurements are plotted in Fig. 2. The uncertainty in PPA for each bin is computed as $\sigma_{\mathrm{PA}} = (\sigma/L)\,(180/\pi)$, where $\sigma = \sqrt{(\sigma_Q^2 + \sigma_U^2)/2}$ represents the combined noise from Stokes Q and U, and L is the linear polarization amplitude. We averaged L/I and $|V|/I$ across the pulse profile to obtain the linear and circular polarization fractions, and uncertainties were computed from the off-pulse standard deviation in the Stokes parameters using error propagation principles. 96 per cent of the bursts are linearly polarized with L/I exceeding 80 per cent. The three bursts with MJDs 60525.65408780 (M79), 60527.63433977 (M248), and 60527.72314018 (M580) exhibit significant circular polarization fractions of 41.7, 45.0, and 37.9 per cent, respectively. A small variation in the PPA angle, on the order of 10°–30°, was observed in 17 out of 80 bursts that yielded a measurable RM.

RM measurements of FRB 20240619D exhibit a consistent increase in magnitude from 2024 June to 2024 September, as illustrated in Fig. 7. The RM values, plotted against MJD in Fig. 7, show a trend that is fitted to a simple linear function, as it is the simplest model. This fit yields a rate of $-1.85 \pm 0.14\,\mathrm{rad\,m^{-2}\,d^{-1}}$, which is consistent with the RM evolution rate of 80 $\mathrm{rad\,m^{-2}}$ over 40 d reported by O. S. Ould-Boukattine et al. (2025a), based on measurements from 2024 July to 2024 August. Together, these results suggest that the immediate environment of the FRB source undergoes dynamic changes, likely driven by local conditions in the magneto-ionic medium. We used the upper limit on $\mathrm{dDM}/\mathrm{d}t \lesssim 0.38\,\mathrm{pc\,cm^{-3}\,d^{-1}}$, as discussed in Section 2.3.4, together with the measured RM evolution of $|\mathrm{dRM}/\mathrm{d}t| = 1.85 \pm 0.14\,\mathrm{rad\,m^{-2}\,d^{-1}}$, to constrain the line-of-sight magnetic field to $|B_\parallel| \gtrsim 6\,\mu\mathrm{G}$, assuming a uniform magnetic field along the line of sight. As we have used an upper limit on the DM rate, the true $B_\parallel$ could be substantially larger if the actual DM variation is smaller than our limit. Comparing to the line-of-sight magnetic field reported by O. S. Ould-Boukattine et al. (2025a), $B_\parallel \approx 0.32 \pm 0.19\,\mathrm{mG}$, we find it to be approximately 50 times our lower limit on $|B_\parallel| \gtrsim 6\,\mu\mathrm{G}$, indicating a highly magnetized environment. Although our estimate excludes extremely small fields (below $\sim 6\,\mu\mathrm{G}$), it does not account for the presence of a strong local magnetic field.

Significant burst-to-burst RM variations are observed within individual days, as shown in Fig. 7. The burst with the largest deviation from its day's median RM occurred on 2024 August 5 (MJD 60527.642858), with a deviation of 90 $\mathrm{rad\,m^{-2}}$ and an RM of $-174 \pm 80\,\mathrm{rad\,m^{-2}}$. Bursts exhibiting significant deviations from the daily median RM, such as this one, are narrow banded (see Fig. 5) and have larger uncertainties in RM.

3 DISCUSSION

3.1 Burst activity and cessation

The detection of bursts from FRB 20240619D over an 80-d interval, followed by a prolonged period of quiescence, presents questions about its activity cycle. Known repeaters such as FRB 20121102A and FRB 20180916B exhibit periodic activity windows with cycles of 159 and 16.35 d, respectively, likely driven by spin modulation, precession, or orbital motion (CHIME/FRB Collaboration 2020; K. M. Rajwade et al. 2020; M. Cruces et al. 2021; C. A. Braga

---

[4] https://github.com/weltevrede/psrsalsa

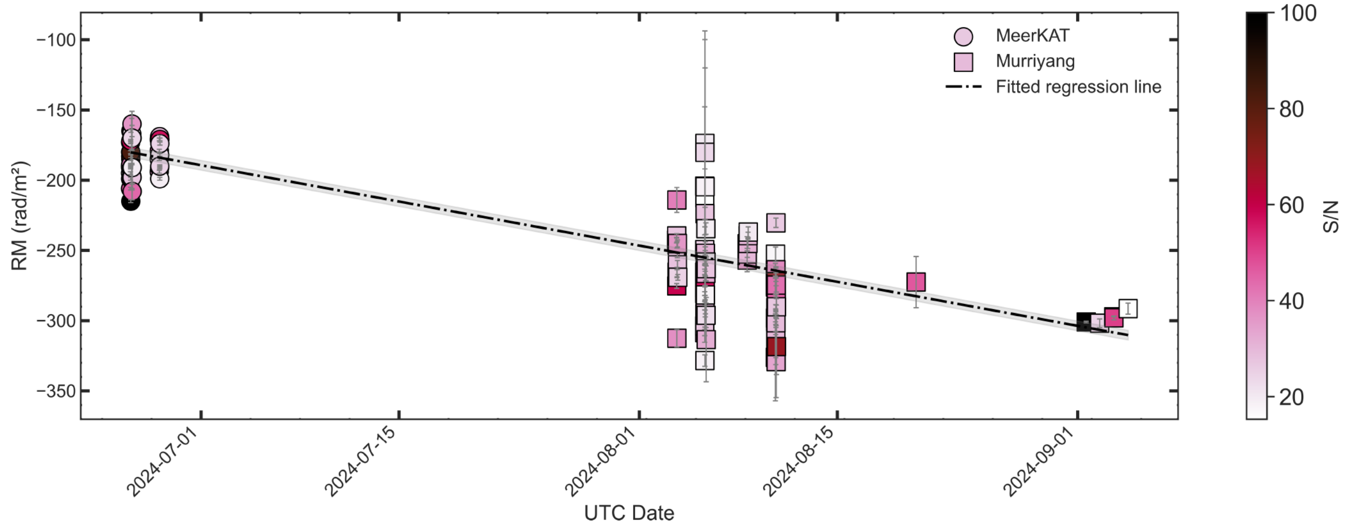

Figure 7. Evolution of RM over MJD of FRB 20240619D. Circles represent data from MeerKAT, and squares represent data from Murriyang. The dashed line represents a weighted linear regression (slope $= 1.85 \pm 0.14\,\mathrm{rad\,m^{-2}\,d^{-1}}$), where weights are proportional to the number of bursts with RM measurements per day divided by the square of RM uncertainties. The grey shaded region indicates the 95 per cent confidence interval, calculated using the weighted standard error of the residuals adjusted by the square root of the weights.

et al. 2025). FRB 20240209A has also been proposed to follow a ∼126-d cycle (A. Pal 2025), further suggesting periodicity as a recurring feature among repeaters. If FRB 20240619D shares such behaviour, continued monitoring is essential to constrain its potential periodicity, which current data suggest may exceed 169 d. What makes FRB 20240619D particularly notable is the time-clustered burst activity, with an estimated ∼161 bursts per hour detected on 2024 August 5, followed by a sharp decline (Fig. 4). This behaviour is reminiscent of FRB 20201124A, observed by FAST (Five-hundred-meter Aperture Spherical Telescope) in 2021 September, during which the burst rate increased exponentially, reaching 381.7 $\mathrm{h^{-1}}$ on 2021 September 28. The rate then sharply declined to zero within 1 d, and no further bursts were detected in the subsequent 3 weeks (D. J. Zhou et al. 2022).

The activity observed in FRB 20240619D may also be interpreted as a non-periodic outburst similar to those seen in magnetars. In the X-ray band, magnetars often exhibit sudden, isolated outbursts caused by magnetic field reconfiguration or crustal fractures, followed by a gradual decay back to quiescence over weeks to years (N. Rea & P. Esposito 2011; F. Coti Zelati et al. 2018; E. Petroff, J. W. T. Hessels & D. R. Lorimer 2022). These events are inherently irregular and not typically periodic. The activity window of FRB 20240619D could also arise from a non-periodic origin. Continued monitoring of FRB 20240619D is essential to determine whether it will re-enter an active phase or remain a singular outburst event.

The burst activity of FRB 20240619D exhibits frequency dependence, with 58 per cent of the total 1138 bursts detected by Murriyang occurring within the 1300–1800 MHz range (Fig. 5). We do not observe any evolution in the preferred emission frequency over time. Other repeating FRBs have also been shown to exhibit different chromatic behaviour in activity. For example, FRB 20180916B shows an activity window that varies with frequency (I. Pastor-Marazuela et al. 2021; M. C. Espinoza-Dupouy et al. 2025). FRB 20201124A shows greater activity at lower frequencies, with a cessation of activity at higher frequencies, as reported by A. V. Bilous et al. (2025). FRB 20240114A shows regular detections in the L band (0.8–2 GHz) and below, while bursts above 2 GHz occur only at later epochs (A. Kumar et al. 2024a). Taken together, these observations suggest that different repeating FRBs may have intrinsically preferred emission frequencies, which are unlikely to be solely due to propagation effects.

3.2 RM increment and implications

The polarimetric properties of FRB 20240619D suggest an evolving magneto-ionic environment around its progenitor. Its absolute RM value increased from 200 to 350 $\mathrm{rad\,m^{-2}}$ over 70 d (2024 June 26 to 2024 September 4), corresponding to a rate of $-1.85 \pm 0.14\,\mathrm{rad\,m^{-2}\,d^{-1}}$, with no detectable DM evolution to a limit of 0.38 $\mathrm{pc\ cm^{-3}\ d^{-1}}$. O. S. Ould-Boukattine et al. (2025a) confirmed coincident temporal variations in RM and also reported changes in DM, less than those we were sensitive to, suggesting that RM evolution in FRB 20240619D can be driven by changes in the electron density (n_e) along the line of sight.

The evolution of RM is not unique to FRB 20240619D. A few other repeating FRBs have shown similar secular RM variations. For example, FRB 20190303A exhibited a steady increase in magnitude of RM from 489 to 701 $\mathrm{rad\,m^{-2}}$ over 137 d (R. Mckinven et al. 2023b), corresponding to a rate of $-1.55\,\mathrm{rad\,m^{-2}\,d^{-1}}$, and FRB 20180916B displayed a notable RM evolution, with the value remaining constant for several months before decreasing at a rate of $0.197\,\mathrm{rad\,m^{-2}\,d^{-1}}$ (R. Mckinven et al. 2023a). In both cases, these RM variations occurred without measurable changes in DM. These examples suggest two possible scenarios: (1) if the regions that contribute significantly to RM and DM are the same, a sufficiently large magnetic field ($|B_\parallel|$) in that region could allow RM to vary without producing detectable changes in DM, provided that it is the electron density that is changing; or (2) most of the contribution to RM and DM originates from physically distinct regions. In the latter case, RM may arise in a highly magnetized, dynamic environment close to the progenitor, while DM remains dominated by a more extended and stable medium along the line of sight. In contrast, RM decrements observed in sources like FRB 20121102A (D. Michilli et al. 2018; A. Plavin et al. 2022; P. Wang et al. 2025) and FRB 20190520B (C. H. Niu et al. 2022; R. Anna-Thomas et al. 2023), which are often accompanied by significant DM variations,

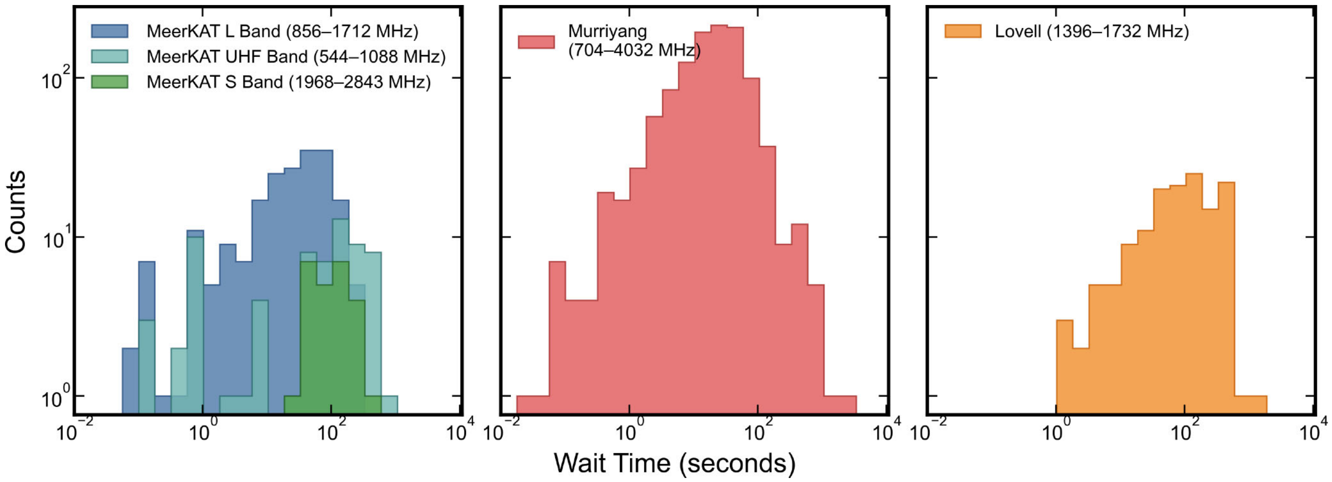

Figure 8. Log–log histograms of burst wait times for FRB 20240619D observed with MeerKAT, Murriyang, and the Lovell telescopes are shown. We calculated burst wait times as the separations between consecutive bursts occurring within the same observing day. The histograms are presented separately for each telescope. For MeerKAT, results are plotted for the UHF (544–1088 MHz), L (856–1712 MHz), and S (1968–2843 MHz) bands. For Murriyang and the Lovell telescopes, the full bandwidths of 704–4032 MHz and 1396–1732 MHz, respectively, were used. Only bursts with fluence greater than 1.6 Jy ms are included in the plot. See Tables 1, 3, and 4 for details on these observations.

are commonly interpreted as resulting from an expanding supernova remnant diluting the local magnetized medium (Y.-P. Yang & B. Zhang 2017; A. L. Piro & B. M. Gaensler 2018). Taken together, the RM variation indicates a dynamic magneto-ionic environment and places FRB 20240619D among repeating FRBs that exhibit variable RM, highlighting the diversity of magneto-ionic environments in FRB environments.

The observed high linear polarization (∼96 per cent of bursts) and occasional circular polarization (∼3 per cent of bursts) of FRB 20240619D are consistent with emission from magnetospheric processes (V. Gajjar et al. 2018; CHIME/FRB Collaboration 2019). The magnitude and rate of increase in RM exceed those typically observed in Galactic pulsars (S. Johnston et al. 2021; R. Mckinven et al. 2023b). This indicates that the source environment is more extreme than typical environments found around pulsars in the Milky Way, and the observed RM variations are not easily explained by normal interstellar medium effects. However, we note that comparably large RM variations have been observed in rare binary systems such as PSR B1259−63, where a pulsar orbits a Be-star companion. In this system, significant changes in RM and DM are observed near periastron as the pulsar's signal propagates through the magnetized stellar wind and circumstellar disc of the companion (A. Melatos, S. Johnston & D. B. Melrose 1995).

3.3 Wait time distribution

The log–log histogram of wait time between adjacent bursts of FRB 20240619D is shown in Fig. 8. We analysed the waiting time distribution of bursts from FRB 20240619D across different frequency ranges to investigate potential clustering behaviour by fitting a Weibull distribution. The Weibull distribution's probability density function is given by

$$f(t; k, \lambda) = \frac{k}{\lambda} \left(\frac{t}{\lambda} \right)^{k-1} \mathrm{e}^{-\left(\frac{t}{\lambda}\right)^k}, \qquad (1)$$

where $t \geq 0$ represents the waiting time between consecutive bursts, $k > 0$ is the shape parameter, and $\lambda > 0$ is the scale parameter. The shape parameter k determines the type of waiting time behaviour: $k = 1$ indicates a Poissonian process (random), $k < 1$ suggests clustering (bursts occur in groups), and $k > 1$ implies regularity (more uniform waiting times). The scale parameter λ reflects the characteristic waiting time.

Fig. 9 shows the density plots of waiting times between adjacent bursts for different frequency ranges, with the observed data compared to the Weibull fit. The Kolmogorov–Smirnov (KS) test was used to assess the goodness of fit for the Weibull distribution. A high p-value, typically greater than 0.05, indicates that the observed data do not significantly differ from the model, suggesting a good fit.

The KS test p-values for our repeater, as shown in Table 5, are all greater than 0.05 across the frequency ranges from 544 to 2724 MHz. This indicates that the wait time distribution of bursts from FRB 20240619D is well described by a Weibull distribution with a shape parameter $k < 1$, confirming clustering in its burst repetition. This finding aligns with clustering in burst arrival times observed in other repeating FRBs, such as FRB 20121102A, FRB 20180916B, and FRB 20201124A (N. Oppermann, H.-R. Yu & U.-L. Pen 2018; CHIME/FRB Collaboration 2020; M. Cruces et al. 2021; G. Q. Zhang et al. 2021; F. Y. Wang, Q. Wu & Z. G. Dai 2023; P. Wang et al. 2024). For FRB 20240619D, this clustering could reflect intrinsic variations in the burst generation mechanism, possibly related to evolving magnetic configurations, as suggested by magnetar models (P. Wang et al. 2024).

3.4 Periodicity search

We carried out a periodicity search for FRB 20240619D by building a Lomb–Scargle periodogram (N. R. Lomb 1976; J. D. Scargle 1982) to the barycentric-corrected arrival times (in MJD) of all bursts detected by MeerKAT, Lovell, and Murriyang. Specifically, we computed the Lomb–Scargle power spectrum over trial periods ranging from 256 µs up to 80 d (80 d corresponds to the interval between the first and last detection). We estimated the false alarm probability (FAP) for each peak using both the analytical approach of R. V. Baluev (2008) and bootstrap resampling (randomly shuffling burst times and recomputing the periodogram 10 000 times). These two methods produced consistent FAP values. Throughout the range of searched

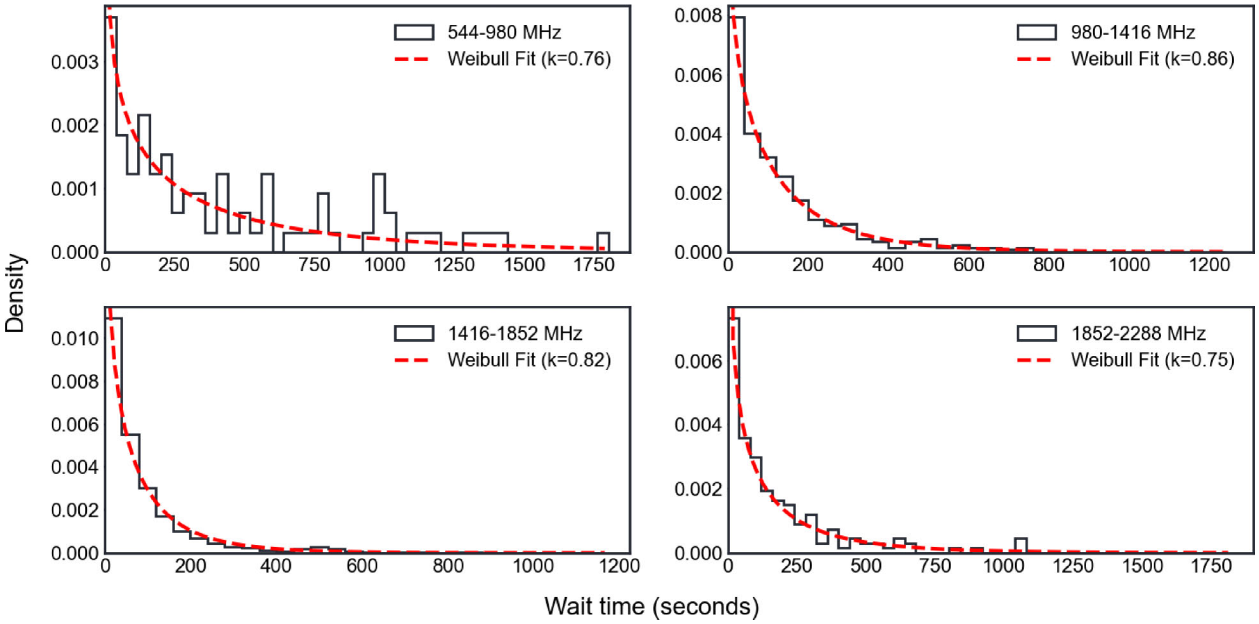

Figure 9. Density plots showing waiting times between adjacent bursts from FRB 20240619D, observed by MeerKAT, Lovell, and Murriyang telescopes across 544–4032 MHz, divided into four frequency bands: 91 bursts (544–980 MHz), 356 bursts (980–1416 MHz), 730 bursts (1416–1852 MHz), and 174 bursts (1852–2288 MHz). This analysis includes only bursts with fluence exceeding 1.6 Jy ms. The 2288–4032 MHz band, with fewer bursts (58 bursts), is excluded. Solid lines represent the observed data, while dashed lines show Weibull fits. The KS test p-values (Table 5) indicate that a Weibull distribution with $k < 1$ provides a good fit, consistent with burst clustering.

Table 5. KS test p-values for Weibull distribution fit to wait time distribution of bursts of FRB 20240619D.

Frequency range (MHz)	Number of bursts	Weibull shape parameter (k)	KS test p-value
544–980	91	0.76	0.45
980–1416	356	0.86	0.67
1416–1852	730	0.82	0.23
1852–2288	174	0.75	0.60

periods, no peak exceeded an FAP threshold of 1 per cent. The data show no evidence of significant periodicity, either on short time-scales (down to 256 µs) or long time-scales. Therefore, we conclude that the arrival times of FRB 20240619D do not exhibit periodicity within our sensitivity limits.

3.5 Fluence distribution of bursts from Murriyang

We estimate the peak flux density of each detected burst using the modified single-pulse radiometer equation (R. J. Dewey et al. 1985):

$$S_{\mathrm{peak}}(\mathrm{S/N}, W_{\mathrm{eq}}) = \frac{\mathrm{S/N\,SEFD}}{\sqrt{b_{\mathrm{eff}} N_{\mathrm{p}} W_{\mathrm{eq}}}}. \tag{2}$$

Based on the modified radiometer equation, we estimate the completeness thresholds of the fluence F_{c} of the UWL following the prescription given by E. F. Keane & E. Petroff (2015) and F. Jankowski et al. (2023). That is, an idealized boxcar-shaped burst of observed equivalent width W_{eq} and given S/N has fluence $F = S_{\mathrm{peak}} W_{\mathrm{eq}}$, with S_{peak} as defined in equation (2). F_{c} is then determined from the widest confidently detected burst of width W^{*}_{eq} as

$$F_{\mathrm{c}} = S_{\mathrm{peak}}\left(\frac{\mathrm{S}}{\mathrm{N}}, W^{*}_{\mathrm{eq}}\right) W^{*}_{\mathrm{eq}}, \tag{3}$$

where S/N $= 7.0$ is the S/N threshold of the search. In our sample, the narrowest burst has an equivalent width of 0.256 ms (burst M1090 at MJD 60532.71261921), while the broadest pulse reaches $W^{*}_{\mathrm{eq}} \approx$ 66 ms (burst M874 at MJD 60532.63559241). Using these computed values from our data set, we obtain $F_{\mathrm{c}} = 1.6$ Jy ms.

The cumulative fluence distribution of bursts with fluence above the completeness limit of 1.6 Jy ms is shown in Fig. 10. In the 704–1396 MHz and 1396–1732 MHz bands, we observe a marginal break in the fluence distribution near 8 Jy ms. Given the small sample of bursts above this threshold in the 704–1396 MHz band, we fit a single power law to the entire range. In the 1396–1732 MHz band, fitting separate power laws above and below 8 Jy ms yields similar indices within uncertainties (-2.07 ± 0.03 and -2.28 ± 0.25), indicating no significant deviation across the break. Therefore, we adopt a single power-law fit for all three frequency bands. This produced a power-law index of $\gamma = -1.82 \pm 0.03$, $\gamma = -2.14 \pm 0.02$, and $\gamma = -2.11 \pm 0.03$ for the frequency ranges 704–1396 MHz, 1396–1732 MHz, and 1732–4032 MHz, respectively. These slopes are consistent with those reported by J. Tian et al. (2025) for FRB 20240619D using MeerKAT observations (first two epochs in Table 1), and are broadly comparable to the results of O. S. Ould-Boukattine et al. (2025a) for the same source using Nançay, Westerbork, and Stockert. At Nançay, O. S. Ould-Boukattine et al. (2025a) reported a steep cumulative fluence distribution ($\gamma_{\mathrm{NRT,C}} = -1.87 \pm 0.03 \pm 0.09$) over 1228–1740 MHz, above a turnover fluence of ∼2.3 Jy ms. In contrast, they found flatter slopes at higher fluences at Westerbork (1207–1335 MHz) and

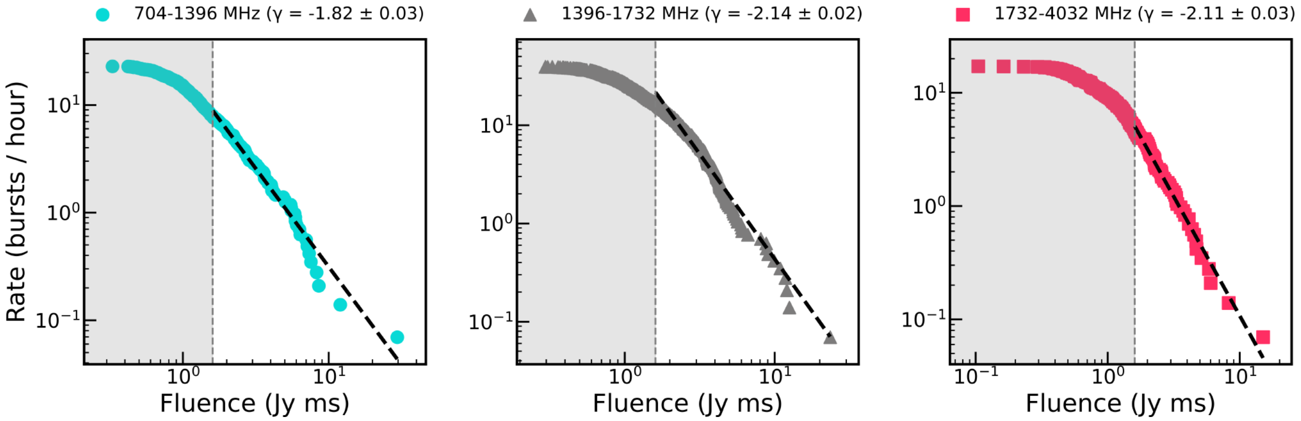

Figure 10. Cumulative burst rate from Murriyang as a function of fluence for different frequency bands. Scatter points represent the observed cumulative burst rate in three frequency bands: 704–1396 MHz (circles), 1396–1732 MHz (triangles), and 1732–4032 MHz (squares). Dashed lines show the best-fitting power-law trends for bursts above the fluence completeness threshold (1.6 Jy ms), with the fitted single power-law indices γ displayed in the legend above each panel. The shaded region indicates fluences below the completeness threshold.

Stockert (1332.5–1430.5 MHz), with $\gamma_{\rm Wb,C} = -0.69 \pm 0.12 \pm 0.15$ and $\gamma_{\rm St,C} = -0.83 \pm 0.15 \pm 0.16$, respectively. These results also support the presence of a break in the fluence distribution. Our fitted indices fall within the steeper regime, indicating that bursts detected with MeerKAT, Murriyang, and Lovell predominantly sample the fainter end of the fluence distribution. These indices are also consistent with other repeaters: FRB 20121102A shows $\gamma \approx -1.5$ to -2.0 (V. Gajjar et al. 2018), FRB 20180916B has $\gamma \approx -1.5$ (CHIME/FRB Collaboration 2020; I. Pastor-Marazuela et al. 2021), and FRB 20201124A exhibits $\gamma \approx -1.8$ to -2.5 (H. Xu et al. 2021; A. V. Bilous et al. 2025). Our distribution does not show evidence of the shallow high-energy tail occasionally reported in extended observing campaigns of active repeaters (D. M. Hewitt et al. 2022; J. N. Jahns et al. 2023; F. Kirsten et al. 2024; Y.-X. Huang et al. 2025; O. S. Ould-Boukattine et al. 2025b, b), suggesting that such features may require prolonged monitoring to detect.

3.6 Microsecond-duration bursts

Among the 1138 detected bursts from FRB 20240619D, we find that 24 exhibit extremely short durations of $\lesssim$256 µs. The detection of such microsecond-scale bursts has significant implications for the physical mechanisms responsible for FRB emission. These bursts are time resolution limited, and it remains uncertain whether they represent genuinely single, intrinsically narrow pulses or are composed of multiple unresolved subburst components, each potentially narrower than 256 µs. Similar microsecond and submillisecond structures have been observed in other repeating FRBs such as FRB 20121102A (D. Michilli et al. 2018; M. P. Snelders et al. 2023) and FRB 20200120E (K. Nimmo et al. 2022). The short durations of these bursts place tight constraints on the size of the emission region. A 256 µs burst corresponds to a light-travel distance of $\lesssim$80 km. Even for a relativistically moving emitter, the observed width reflects the central engine time-scale (B. Zhang 2023). This compactness implies coherent emission likely originating near the neutron star surface. The brightness temperature estimates for such bursts often exceed 10^{35} K, reinforcing the need for a coherent emission mechanism (W. Farah et al. 2018).

Several physical models have been proposed to explain the origin of such short bursts. One leading model is coherent curvature radiation from charged bunches in a strongly magnetized magnetosphere, possibly triggered by starquakes or magnetic reconnection events in a magnetar (P. Beniamini & P. Kumar 2020; W. Lu, P. Beniamini & P. Kumar 2022). One key argument against this idea is the absence of a clear explanation for why the instability would fragment the emission into microshots, yet leave the broader emission components just milliseconds later unaffected. It is also important to compare these results with one-off FRBs. For example, FRB 20181223A showed a ~30 µs component embedded within a 0.5 ms envelope (W. Farah et al. 2018). This suggests that such short bursts are not exclusive to repeaters and that the underlying emission mechanism may be common across FRB populations.

3.7 Non-detection of a persistent radio source

No PRS has been detected in association with FRB 20240619D with MeerKAT and ATCA covering a frequency range between 0.5 and 12 GHz. This sets it apart from other well-studied repeaters, such as FRB 20121102A (S. Chatterjee et al. 2017; B. D. Metzger, E. Berger & B. Margalit 2017), FRB 20190520B (C. H. Niu et al. 2022), FRB 20201124A (G. Bruni et al. 2024), and FRB 20240114A (Y. Bhusare et al. 2025), all of which have been associated with PRSs. For FRB 20240619D, this could indicate a progenitor system, such as a magnetar, that lacks the necessary conditions to form a detectable nebula, possibly due to a lower ambient density, an older age, or a distinct evolutionary history (Y. Levin et al. 2020).

Alternatively, the absence of a PRS may suggest that the FRB 20240619D activity is not powered by a continuously active central engine, but rather arises from episodic or intermittent processes. One possibility is that the PRS exists but exhibits different spectral properties as seen for the PRS associated with FRB 20201124A (H. Xu et al. 2021), such as an inverted spectrum, which would make it more detectable at higher radio frequencies. However, the non-detection of a PRS, including with ATCA up to 12 GHz, raises the possibility that it may be intrinsically faint or absent, although our ATCA limits are not sufficiently constraining to rule out a PRS with flux density below 1.2 mJy. We therefore recommend high-frequency radio imaging (e.g. $\gtrsim$12 GHz) to search for a faint PRS and to place tighter constraints on the local environment and progenitor properties of FRB 20240619D.

3.7.1 Inferred luminosity of a potential PRS

To estimate the luminosity of a potential PRS associated with FRB 20240619D, we adopt the empirical relation from Y.-P. Yang et al. (2020), which assumes that the observed RM primarily originates from the region responsible for the persistent emission. The redshift is estimated using the Macquart relation (J. P. Macquart et al. 2020), assuming a DM excess of 348.4 $\mathrm{pc\,cm^{-3}}$, derived after subtracting the Galactic contribution. This yields a redshift estimate of $z = 0.38^{+0.10}_{-0.22}$.

Among all epochs, the highest median RM (computed from multiple bursts during a single day) is $\mathrm{RM_{obs}} = 301.8 \pm 3.0\,\mathrm{rad\,m^{-2}}$ (see Table 3). According to the formalism presented by Y.-P. Yang et al. (2020, 2022), the luminosity of the PRS can be approximated as

$$L_\nu \simeq 5.7 \times 10^{28}\,\mathrm{erg\,s^{-1}\,Hz^{-1}} \times \zeta_e \gamma_{\mathrm{th}}^2 \left(\frac{|\mathrm{RM}|}{10^4\,\mathrm{rad\,m^{-2}}}\right)\left(\frac{R}{10^{-2}\,\mathrm{pc}}\right), \tag{4}$$

where ζ_e is the ratio of the number density of relativistic (synchrotron-emitting) electrons to that of the thermal (RM-contributing) electrons, γ_{th} is the Lorentz factor of the thermal electrons, and R represents the size of the persistent emission region. We adopt $R \sim c\Delta t_{\mathrm{var}} \approx 10^{-2}$ pc, assuming variability on ~10 d time-scales.

The parameter $\zeta_e \gamma_{\mathrm{th}}^2$ is observationally constrained to lie between ~0.1 and 10 based on known PRSs associated with FRBs such as 20121102A, 20190520B, and 20201124A (G. Bruni et al. 2024).

To isolate the RM contribution intrinsic to the FRB's local environment, we decompose the observed RM as follows:

$$\mathrm{RM_{obs}} = \mathrm{RM_{ion}} + \mathrm{RM_{MW}} + \mathrm{RM_{MW,halo}} + \mathrm{RM_{IGM}} + \mathrm{RM_{host}}. \tag{5}$$

Here, $\mathrm{RM_{ion}}$ ($\sim\pm 1\,\mathrm{rad\,m^{-2}}$; C. Sobey et al. 2019) is the ionospheric contribution, which we neglect due to its minimal impact. Similarly, $\mathrm{RM_{IGM}}$ is assumed to be negligible due to the weak magnetic fields in the intergalactic medium (typically <21 nG; V. Ravi et al. 2016) and potential field reversals.

The Galactic RM foreground, comprising $\mathrm{RM_{MW}} + \mathrm{RM_{MW,halo}}$, is estimated from the interpolated all-sky RM map of S. Hutschenreuter et al. (2022), yielding $27.8 \pm 9.1\,\mathrm{rad\,m^{-2}}$ in the direction of FRB 20240619D. After correcting for Galactic foregrounds and applying a $(1+z)^2$ redshift correction, we derive a host-frame RM of $191 \pm 9\,\mathrm{rad\,m^{-2}}$.

Substituting this into equation (4), and allowing for the range of $\zeta_e \gamma_{\mathrm{th}}^2 \sim 0.1$–10, we estimate the PRS luminosity to be in the range $L_\nu \simeq (1\text{–}100) \times 10^{25}\,\mathrm{erg\,s^{-1}\,Hz^{-1}}$.

At the luminosity distance corresponding to $z = 0.38$, this translates to a flux density of ~0.002–0.205 μJy. If the Yang relation (equation 4) between RM and PRS flux density holds, detecting such a PRS is far beyond the detection limits of current radio telescopes, including MeerKAT and the VLA (Very Large Array), and would require higher sensitivities achievable only with future instruments like the full Square Kilometre Array.

4 CONCLUSIONS

We present a comprehensive multitelescope study of the hyperactive repeater FRB 20240619D, aimed at understanding the spectro-temporal evolution of its burst activity and properties. We also search for the presence of a PRS, which is key to understanding its progenitor, local environment, and placing it within the broader population of hyperactive repeaters. Our high-cadence follow-up of FRB 20240619D using MeerKAT, Murriyang, and Lovell confirmed its hyperactive nature, with a total of 1539 bursts detected. The burst rate peaked at an estimated 161 bursts per hour on 2024 August 5, followed by a sharp decline, with no bursts detected during the subsequent observation on 2024 September 16. The burst activity also exhibited strong frequency dependence, with 61 per cent of bursts detected between 1.3 and 1.8 GHz. The magnitude of RM exhibits a steady increase at a rate of $\sim 1.85 \pm 0.14\,\mathrm{rad\,m^{-2}\,d^{-1}}$, indicating an evolving magneto-ionic environment near the source. In contrast, our DM measurements show no discernible trend, indicating that any density-driven DM variations are below our measurement uncertainties.

Despite intensive follow-up with MeerKAT and ATCA, no PRS has yet been detected. This result is inconsistent with models that associate hyperactive repeaters with young magnetars embedded in dense environments (B. Margalit, E. Berger & B. D. Metzger 2019), and could favour a progenitor in a lower density medium, possibly at a more evolved stage (Y. Levin et al. 2020). Alternatively, a faint or spectrally inverted PRS may still exist, which would motivate deeper radio imaging at higher frequencies (e.g. $\gtrsim$12 GHz).

The burst activity of FRB 20240619D ceased after ~80 d of hyperactivity, and the arrival times show clustering, inconsistent with a simple Poisson process. This hints at episodic or possibly periodic behaviour, similar to a few other repeaters. These findings emphasize the diverse phenomenology of repeating FRBs and the need for continued high-cadenced polarimetric and wideband monitoring to constrain their progenitor systems and environments.

ACKNOWLEDGEMENTS

The authors thank the directors, staff, and operators of the MeerKAT, Murriyang, Australia Telescope Compact Array (ATCA), and Lovell telescopes for their support and for enabling prompt scheduling and execution of the observations. KS thanks Pravir Kumar for developing the subbanded search pipeline used in processing the Murriyang data, and Adam Deller and Paul Demorest for useful discussions, which helped in interpreting the imaging results related to the search for a persistent radio source. KS would like to thank Shi Dai for support and guidance with the polarization calibration of the Murriyang data. The authors would like to thank the anonymous reviewer for detailed comments that greatly improved the manuscript.

This work used data from the MeerKAT telescope, operated by the South African Radio Astronomy Observatory (SARAO), a facility of the National Research Foundation, an agency of the Department of Science and Innovation. SARAO acknowledges the ongoing advice and calibration of GPS systems by the National Metrology Institute of South Africa (NMISA) and the time–space reference systems department of the Paris Observatory. The FBFUSE (Filterbanking Beamformer User Supplied Equipment) beamforming cluster was funded, installed, and operated by the Max-Planck-Institut für Radioastronomie and the Max-Planck-Gesellschaft. This scientific work used data obtained from Murriyang and ATCA telescopes. Murriyang and ATCA are part of the Australia Telescope National Facility, which is funded by the Australian Government for operation as a National Facility managed by CSIRO. This study analysed data obtained from the Lovell telescope at the Jodrell Bank Observatory, a facility of the University of Manchester. We acknowledge the support of the Nuffield Foundation and the government for the construction and operation of the telescope.

This project has received funding from the European Research Council (ERC) under the European Union's Horizon 2020 Framework Programme (grant agreement no. 694745). MC and KS acknowledge support from the Australian Research Council Discovery Early Career Research Award (project number DE220100819). IP-M acknowledges funding from an NWO Rubicon Fellowship, project number 019.221EN.019. Parts of this research were conducted by the Australian Research Council Centre of Excellence for Gravitational Wave Discovery (OzGrav), project number CE230100016.

DATA AVAILABILITY

The MeerKAT, Murriyang, ATCA, and Lovell data underlying this paper will be shared on reasonable request to the corresponding author.

REFERENCES

Agarwal D., Aggarwal K., Burke-Spolaor S., Lorimer D. R., Garver-Daniels N., 2020, MNRAS, 497, 1661
Anna-Thomas R. et al., 2023, Science, 380, 599
Baluev R. V., 2008, MNRAS, 385, 1279
Barsdell B. R., 2012, PhD thesis, Swinburne University of Technology, Australia
Beniamini P., Kumar P., 2020, MNRAS, 498, 651
Beniamini P., Wadiasingh Z., Metzger B. D., 2020, MNRAS, 496, 3390
Bethapudi S., Spitler L. G., Main R. A., Li D. Z., Wharton R. S., 2023, MNRAS, 524, 3303
Bhusare Y., Maan Y., Kumar A., 2025, ApJ, 993, 234
Bilous A. V., van Leeuwen J., Maan Y., Pastor-Marazuela I., Oostrum L. C., Rajwade K. M., Wang Y. Y., 2025, A&A, 696, A194
Braga C. A., Cruces M., Cassanelli T., Espinoza-Dupouy M. C., Rodriguez L., Spitler L. G., Vera-Casanova J., Limaye P., 2025, A&A, 693, A40
Bruni G. et al., 2024, Nature, 632, 1014
Bruni G. et al., 2025, A&A, 695, L12
Caleb M., Stappers B. W., Rajwade K., Flynn C., 2019, MNRAS, 484, 5500
Chatterjee S. et al., 2017, Nature, 541, 58
CHIME/FRB Collaboration, 2019, Nature, 566, 230
CHIME/FRB Collaboration, 2020, Nature, 582, 351
CHIME/FRB Collaboration, 2023, ApJ, 947, 83
Cordes J. M., Chatterjee S., 2019, ARA&A, 57, 417
Coti Zelati F., Rea N., Pons J. A., Campana S., Esposito P., 2018, MNRAS, 474, 961
Cruces M. et al., 2021, MNRAS, 500, 448
Dai S. et al., 2019, ApJ, 874, L14
Dewey R. J., Taylor J. H., Weisberg J. M., Stokes G. H., 1985, ApJ, 294, L25
Espinoza-Dupouy M. C., Cruces M., Cassanelli T., Braga C. A., Bermúdez E., Vera-Casanova J., 2025, preprint (arXiv:2507.04609)
Farah W. et al., 2018, MNRAS, 478, 1209
Feng Y. et al., 2022, Science, 375, 1266
Feng Y. et al., 2024, ApJ, 974, 296
Flesch E. W., 2015, Publ. Astron. Soc. Aust., 32, e010
Fonseca E. et al., 2020, ApJ, 891, L6
Gajjar V. et al., 2018, ApJ, 863, 2
Hewitt D. M. et al., 2022, MNRAS, 515, 3577
Hewitt D. M. et al., 2023, MNRAS, 526, 2039
Heywood I., 2020, Astrophysics Source Code Library, record ascl:2009.003
Hilmarsson G. H., Spitler L. G., Main R. A., Li D. Z., 2021, MNRAS, 508, 5354
Hobbs G. et al., 2019, Publ. Astron. Soc. Aust., 36, e023
Hotan A. W., van Straten W., Manchester R. N., 2004, Publ. Astron. Soc. Aust., 21, 302
Huang Y.-X. et al., 2025, Res. Astron. Astrophys., 25, 085009
Hutschenreuter S. et al., 2022, A&A, 657, A43
Ioka K., Zhang B., 2020, ApJ, 893, L26
Jahns J. N. et al., 2023, MNRAS, 519, 666
Jankowski F. et al., 2023, MNRAS, 524, 4275
Jiang J.-C. et al., 2022, Res. Astron. Astrophys., 22, 124003
Johnston S. et al., 2021, MNRAS, 502, 1253
Keane E. F., Petroff E., 2015, MNRAS, 447, 2852
Kirsten F. et al., 2024, Nat. Astron., 8, 337
Kumar P. et al., 2021a, MNRAS, 500, 2525
Kumar P., Shannon R. M., Moss V., Qiu H., Bhandari S., 2021b, Astron. Telegram, 14502, 1
Kumar P., Shannon R. M., Lower M. E., Bhandari S., Deller A. T., Flynn C., Keane E. F., 2022, MNRAS, 512, 3400
Kumar A., Maan Y., Bhusare Y., 2024a, ApJ, 977, 177
Kumar A., Maan Y., Bhusare Y., 2024b, Astron. Telegram, 16452, 1
Kumar A., Panda U., Bhusare Y., Maan Y., Roy J., Bhattacharyya S., Dudeja C., Lal B., 2024c, Astron. Telegram, 16745, 1
Lanman A. E. et al., 2022, ApJ, 927, 59
Levin Y., Beloborodov A. M., Bransgrove A., 2020, ApJ, 895, L30
Li D. et al., 2021, Nature, 598, 267
Liu X. et al., 2025, ApJ, 988, 175
Lomb N. R., 1976, Ap&SS, 39, 447
Lorimer D. R., Bailes M., McLaughlin M. A., Narkevic D. J., Crawford F., 2007, Science, 318, 777
Lower M. E., Shannon R. M., Johnston S., Bailes M., 2020, ApJ, 896, L37
Lu W., Beniamini P., Kumar P., 2022, MNRAS, 510, 1867
Luo R. et al., 2020, Nature, 586, 693
Mckinven R. et al., 2023a, ApJ, 949, 28
Mckinven R. et al., 2023b, ApJ, 951, 82
McMullin J. P., Waters B., Schiebel D., Young W., Golap K., 2007, in Shaw R. A., Hill F., Bell D. J., eds, ASP Conf. Ser. Vol. 376, Astronomical Data Analysis Software and Systems XVI. Astron. Soc. Pac., San Francisco, p. 127
Macquart J. P. et al., 2020, Nature, 581, 391
Margalit B., Metzger B. D., 2018, ApJ, 868, L4
Margalit B., Berger E., Metzger B. D., 2019, ApJ, 886, 110
Melatos A., Johnston S., Melrose D. B., 1995, MNRAS, 275, 381
Men Y., Barr E., 2024, A&A, 683, A183
Metzger B. D., Berger E., Margalit B., 2017, ApJ, 841, 14
Metzger B. D., Margalit B., Sironi L., 2019, MNRAS, 485, 4091
Michilli D. et al., 2018, Nature, 553, 182
Mohan N., Rafferty D., 2015, Astrophysics Source Code Library, record ascl:1502.007
Moroianu A. M. et al., 2025, preprint (arXiv:2509.05174)
Ng C. et al., 2025, ApJ, 982, 154
Nimmo K. et al., 2022, Nat. Astron., 6, 393
Niu C. H. et al., 2022, Nature, 606, 873
Niu J. R. et al., 2024, ApJ, 972, L20
Oppermann N., Yu H.-R., Pen U.-L., 2018, MNRAS, 475, 5109
Ould-Boukattine O. S. et al., 2025b, MNRAS, 545, staf1937
Ould-Boukattine O. S. et al., 2025a, preprint (arXiv:2509.16374)
Pal A., 2025, ApJ, 983, L15
Panda U., Bhattacharyya S., Dudeja C., Kudale S., Roy J., 2024, Astron. Telegram, 16494, 1
Pastor-Marazuela I. et al., 2021, Nature, 596, 505
Petroff E., Hessels J. W. T., Lorimer D. R., 2022, A&AR, 30, 2
Piro A. L., Gaensler B. M., 2018, ApJ, 861, 150
Plavin A., Paragi Z., Marcote B., Keimpema A., Hessels J. W. T., Nimmo K., Vedantham H. K., Spitler L. G., 2022, MNRAS, 511, 6033
Pleunis Z. et al., 2021a, ApJ, 911, L3
Pleunis Z. et al., 2021b, ApJ, 923, 1
Rajwade K. M. et al., 2020, MNRAS, 495, 3551
Rajwade K. M. et al., 2022, MNRAS, 514, 1961
Ravi V. et al., 2016, Science, 354, 1249
Rea N., Esposito P., 2011, in Torres D., Rea N., eds, High-Energy Emission from Pulsars and their Systems. Springer-Verlag, Berlin, p. 247
Sault R. J., Teuben P. J., Wright M. C. H., 1995, in Shaw R. A., Payne H. E., Hayes J. J. E., eds, ASP Conf. Ser. Vol. 77, Astronomical Data Analysis Software and Systems IV. Astron. Soc. Pac., San Francisco, p. 433
Scargle J. D., 1982, ApJ, 263, 835
Seymour A., Michilli D., Pleunis Z., 2019, Astrophysics Source Code Library, record ascl:1910.004
Shin K. et al., 2025, preprint (arXiv:2505.13297)
Snelders M. P. et al., 2023, Nat. Astron., 7, 1486
Sobey C. et al., 2019, MNRAS, 484, 3646
Thornton D. et al., 2013, Science, 341, 53

Tian J. et al., 2024a, MNRAS, 533, 3174
Tian J. et al., 2024b, Astron. Telegram, 16690, 1
Tian J. et al., 2025, MNRAS, 540, 1685
van Straten W., Bailes M., 2011, Publ. Astron. Soc. Aust., 28, 1
Wang F. Y., Wu Q., Dai Z. G., 2023, ApJ, 949, L33
Wang P., Song L.-M., Xiong S.-L., Zhao X.-Y., Wang J., 2024, ApJ, 975, 188
Wang P. et al., 2025, preprint (arXiv:2507.15790)
Wardle J. F. C., Kronberg P. P., 1974, ApJ, 194, 249
Wilson W. E. et al., 2011, MNRAS, 416, 832
Xu H. et al., 2021, Astron. Telegram, 14518, 1
Yang Y.-P., Zhang B., 2017, ApJ, 847, 22
Yang Y.-P., Li Q.-C., Zhang B., 2020, ApJ, 895, 7
Yang Y.-P., Lu W., Feng Y., Zhang B., Li D., 2022, ApJ, 928, L16
Zhang B., 2023, Rev. Mod. Phys., 95, 035005
Zhang G. Q., Wang P., Wu Q., Wang F. Y., Li D., Dai Z. G., Zhang B., 2021, ApJ, 920, L23
Zhang Y.-K. et al., 2023, ApJ, 955, 142
Zhang X., Yu W., Yan Z., Xing Y., Zhang B., 2025, preprint (arXiv:2501.14247)
Zhou D. J. et al., 2022, Res. Astron. Astrophys., 22, 124001

This paper has been typeset from a TEX/LATEX file prepared by the author.